

Marine gravity anomaly from Geosat and ERS 1 satellite altimetry

David T. Sandwell

Institute of Geophysics and Planetary Physics, Scripps Institution of Oceanography, University of California, La Jolla

Walter H. F. Smith

Geosciences Laboratory, NOAA, Silver Spring, Maryland

Abstract. Closely spaced satellite altimeter profiles collected during the Geosat Geodetic Mission (~6 km) and the ERS 1 Geodetic Phase (8 km) are easily converted to grids of vertical gravity gradient and gravity anomaly. The long-wavelength radial orbit error is suppressed below the noise level of the altimeter by taking the along-track derivative of each profile. Ascending and descending slope profiles are then interpolated onto separate uniform grids. These four grids are combined to form comparable grids of east and north vertical deflection using an iteration scheme that interpolates data gaps with minimum curvature. The vertical gravity gradient is calculated directly from the derivatives of the vertical deflection grids, while Fourier analysis is required to construct gravity anomalies from the two vertical deflection grids. These techniques are applied to a combination of high-density data from the dense mapping phases of Geosat and ERS 1 along with lower-density but higher-accuracy profiles from their repeat orbit phases. A comparison with shipboard gravity data shows the accuracy of the satellite-derived gravity anomaly is about 4–7 mGal for random ship tracks. The accuracy improves to 3 mGal when the ship track follows a Geosat Exact Repeat Mission track line. These data provide the first view of the ocean floor structures in many remote areas of the Earth. Some applications include inertial navigation, prediction of seafloor depth, planning shipboard surveys, plate tectonics, isostasy of volcanoes and spreading ridges, and petroleum exploration.

Introduction

Radar altimeter measurements of the marine geoid collected during the Seasat altimeter mission gave marine geodesists and geophysicists a hope of uncovering the details in the gravity field over all the ocean basins [Haxby *et al.*, 1983]. However, because of insufficient track density, it has taken 16 years for the full potential of the satellite altimeter method to be realized. The high-density coverage obtained by ERS 1 during its geodetic mapping phase (April 1994 to March 1995) prompted the U.S. Navy to declassify all of the Geosat altimeter data on June 22, 1995. We are grateful to the European Space Agency for extending the ERS 1 mapping phase so that an equatorial ground track spacing of 8 km could be completed. The combination of these two high-density data sets provided the first detailed view of all the ocean basins at a 10-km resolution. Considering the sparse shipboard coverage of many ocean areas [Smith, 1993], these new altimeter data are arguably the most important marine geology and geophysics data set collected over the past decade.

The focus of this paper is on the efficient recovery of marine gravity anomalies and other derivatives of the potential using data from satellite altimeters having different orbital inclinations and different noise characteristics; no attempt is made to recover sea surface topography (i.e., geoid height plus ocean dynamic topography). After an introduction to radar altimetry and its inherent limitations, we discuss data availability and our recipe for constructing gridded gravity anomalies from altimeter profiles. The method (recipe) presented here is based largely on

previous work [Heiskanen and Moritz, 1967; Briggs, 1974; Haxby *et al.*, 1983; Sandwell, 1984; Freedman and Parsons, 1986; Haxby and Weissel, 1986; Roest, 1987; Smith and Wessel, 1990; Rummel and Haagmans, 1990; Haxby and Hayes, 1991; Sandwell, 1992; Laxon and McAdoo, 1994; Hwang and Parsons, 1996]. We then assess the quality of the gridded data and suggest possible ways to improve the resolution of the gravity field along stacked profiles. Finally, we provide a tour of the gravity field of the oceans and point out a few of the new and interesting features. We do not attempt to review other methods for recovery of short-wavelength gravity information from satellite altimetry [e.g., Wakker *et al.*, 1993; Cazenave *et al.*, 1995; Andersen *et al.*, 1995; Hwang and Parsons, 1995] but instead focus on our recipe, discuss how it was developed, and explain why certain processes are used. Over the next months and years our recipe may undergo revisions, and perhaps others will devise better recipes.

This research has two main components. The first component, presented in this manuscript, is a traditional journal article with appendices. Appendix A covers the relationship between geoid height, vertical deflection, gravity gradient, and gravity anomaly. Appendix B covers the statistical method to estimate north and east vertical deflections from along-track slopes. Appendix C has the derivation of analytic formulae to calculate the approximate satellite position and velocity as a function of time since equator crossing and latitude. The second part of our research is more suitable for electronic media and will be submitted for publication to *Earth Interactions*. It contains many color images of the marine gravity field (<http://topex.ucsd.edu>); the images are layered so the reader can zoom in on features of interest. In addition, the companion electronic article contains all of the computer code used to construct the results shown in both papers as well as links to files of gridded gravity anomaly, vertical gravity gradient, and high-quality postscript plots of gravity

Copyright 1997 by the American Geophysical Union.

Paper number 96JB03223.
0148-0227/97/96JB-03223\$09.00

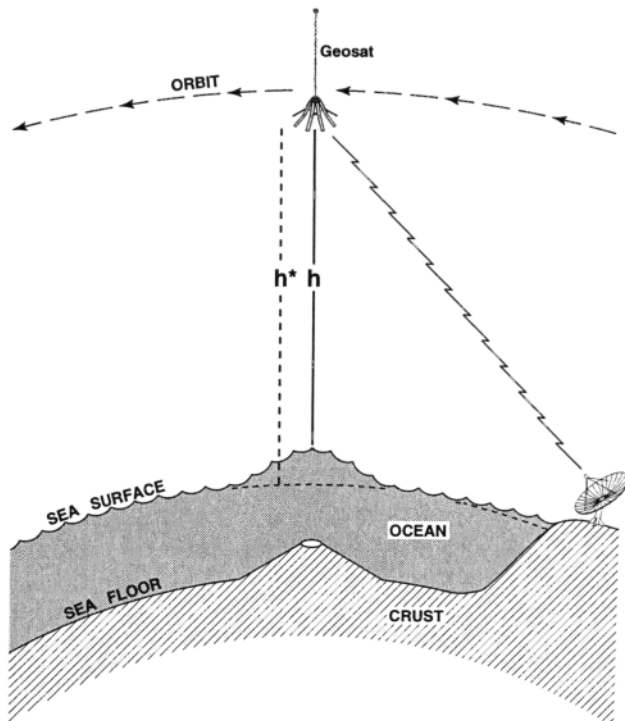


Figure 1. A pulse-limited radar altimeter orbits at an altitude of about 800 km and measures the distance to the closest ocean surface by recording the travel time of a pulse. A global tracking network along with precise orbit calculations based on the JGM-3 gravity model [Nerem *et al.*, 1994] is used to establish the height of the satellite above the reference ellipsoid (dashed curve). We assume the sea surface height above the ellipsoid is equal to the geoid height so permanent sea surface slopes associated with currents will appear as false anomalies in our gravity solution.

anomaly at the General Bathymetric Chart of the Oceans map scale. The companion electronic paper also contains links to scripts illustrating the use of the gravity anomaly grids with GMT software [Wessel and Smith, 1995].

Satellite Altimetry

A satellite altimeter uses a pulse-limited radar to measure the altitude of the satellite above the closest sea surface point to a very high precision (Figure 1). Global precise tracking coupled with orbit dynamic calculations provide an independent measurement of the height of the satellite above the ellipsoid. The difference between these two measurements is equal to the instantaneous sea surface height minus any delays in the propagation of the radar echo due to the ionosphere and troposphere. There are many errors in these measurements that are discussed and evaluated in a number of excellent papers [Nerem *et al.*, 1994; Tapley *et al.*, 1994; Ma *et al.*, 1994; Visser *et al.*, 1993]. Most of these errors occur over length scales of greater than a few hundred kilometers. They are important for precise oceanographic studies or studies where the geoid height is needed. However, because we are only interested in the gradient of the sea surface, the short-wavelength altimeter noise dominates the error budget.

There are at least two factors that impose limits on the accuracy and resolution of gravity field recovery from satellite altimetry. First the ocean depth (~4 km) attenuates the short-

wavelength gravity signals (equation (A9)). Consider an anomaly on the ocean floor with a 16-km wavelength and a 15-mGal amplitude (i.e., a typical value for oceans). On the ocean surface this anomaly will be reduced to 3.1 mGal by upward continuation. The second limitation is due to the short-wavelength noise from ocean surface waves (typically > 1 m). The radar pulse reflects from an area of ocean surface (footprint) that grows with increasing sea state [Stewart, 1985]. The superposition of the reflections from this area stabilizes the shape of the echo, but it also smooths the echo so that the timing of its leading edge is more uncertain. By averaging many echoes (1000 Hz) over multiple repeat cycles, one can achieve a 10 to 20-mm range precision [Noreus 1995; Yale *et al.*, 1995]. Over a distance of 4 km (i.e., 1/4 wavelength) this corresponds to a sea surface slope error of 4 μ rad and a gravity error of about 4 mGal (Appendix A). The combination of these two limitations makes it difficult to improve the resolution. Consider trying to improve the resolution by a factor of 2, upward continuation will attenuate the signal by an additional factor of $e^2 = 7.4$, so assuming a Gaussian error distribution, the number of measurements must be increased by a factor of $e^4 = 55$. At longer wavelengths or in shallower water the situation is not as bad, but nevertheless the roughness of the ocean surface limits the accuracy of the short-wavelength slope estimate. We show that ocean tides, which can also have a short-wavelength component especially on the continental shelves, are a third limiting factor in the recovery of the gravity field. It is surprising that other factors such as basin-scale dynamic ocean topography are not important; in this case the slope of this error is usually low (e.g., 1 m over say 3000 km which translates into 0.33 mGal). Sharper oceanographic steps associated with western boundary currents can be a significant error source [Gille, 1994].

The repeat period of the satellite orbit governs the spacing of the altimeter tracks on the ocean surface (Figure 2). Very long repeat cycles such as 168-day ERS 1 geodetic phase or the non-repeat (drifting) orbit of the Geosat/Geodetic Mission (Geosat/GM) provide the high-density coverage needed for complete resolution of the gravity field. The shorter repeat periods of 10 days for TOPEX, 17 days for Geosat, and 35 days for ERS 1 do not provide dense track coverage. However, the repeated profiles can be averaged to improve the signal-to-noise ratio as well as to assess the noise properties of the altimeter measurements. Here we do not use the TOPEX or POSEIDON altimeter measurements because the wide track spacing provides little new information.

Along-Track Preprocessing

The starting point for the Geosat data are geophysical data records (GDR) from National Oceanographic Data Center [Cheney *et al.*, 1991] where the orbital information for the Geodetic Mission data was upgraded to the Joint Gravity Model 3 (JGM-3) orbits [Nerem *et al.*, 1994]. The ERS 1 ocean product (OPR) data [Dumont *et al.*, 1995] were used with their original orbits as were the Geosat Exact Repeat Mission (Geosat/ERM) data. The along-track processing of the raw geophysical data records consists of a number of steps: edit, apply corrections, divide into passes, low-pass filter, resample at 5 Hz, and differentiate. The editing criteria were established by examining raw altimeter data from a variety of satellites and under a variety of conditions. Care is taken to remove outliers in areas of ice or land prior to any filtering. In the open ocean we try to retain all points except when the shape of the return pulse suggests that the

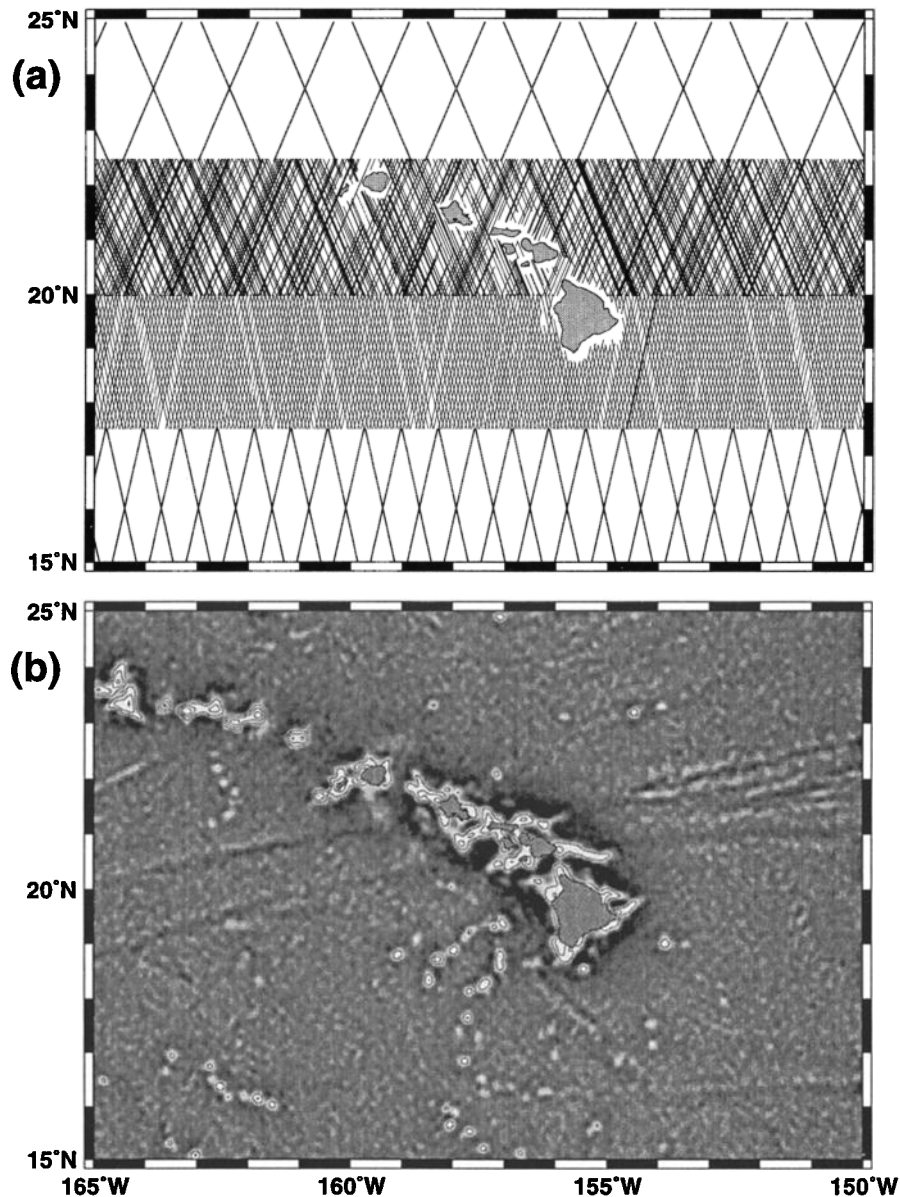


Figure 2. (a) Tracks of stacked Geosat/ERM (17-day repeat cycle) (22.5°-25° N), Geosat/GM (20°-22.5° N), ERS 1 Geodetic Phase (168-day repeat cycle) (17.5°-20° N), and stacked ERS 1 (35-day repeat cycle) (15°-17.5°N). These tracks show data remaining after editing and filtering. (b) Vertical gravity gradient (i.e., curvature of ocean surface) around Hawaii derived from all four data sets. Contours at 50 and 100 Eotvos units are shown to highlight seamount/island signatures.

significant wave height (SWH) is high; these data are usually noisy [Yale *et al.*, 1995]. Unfortunately, much of our documentation on the choice of edit thresholds is located in a variety of old notebooks and tapes and thus cannot be completely justified.

Our editing approach examines the individual 10-Hz samples in relation to the best fit straight line through the 10 points as described by Cheney *et al.* [1991]. If the rms about the line is greater than 0.15 m for Geosat (0.25 m for ERS 1) or the SWH exceeds 8 m for Geosat (6 m for ERS 1), then all 10 points are edited. In addition, a new 2-min gridded land/water mask was developed using the Generic Mapping Tools (GMT) software package [Wessel and Smith, 1995] to eliminate frames near land where stray echos can contaminate the ocean data, especially when low-pass filters are applied. Finally, each 10-Hz point was

compared with the best fit line. If its deviation from the line was more than 5 times the rms about the line, then the point was eliminated, a new best fit line was computed, and the points were tested again until they all passed or until only six points remained.

Our primary focus is on the recovery of the short-wavelength gravity field information, and thus not all corrections are relevant or even useful. For example, corrections based on global models (i.e., wet troposphere, dry troposphere, ionosphere, and inverted barometer) typically do not have wavelength components shorter than 1000 km, and if their amplitude variations are less than 1 m they do not contribute more than 1 μ rad to the noise. Some corrections such as the electromagnetic bias can actually add noise [Gille, 1994]. We have found that the most important correction to the sea surface slope is the ocean tide and have determined that the Center for Space Research (CSR) composite

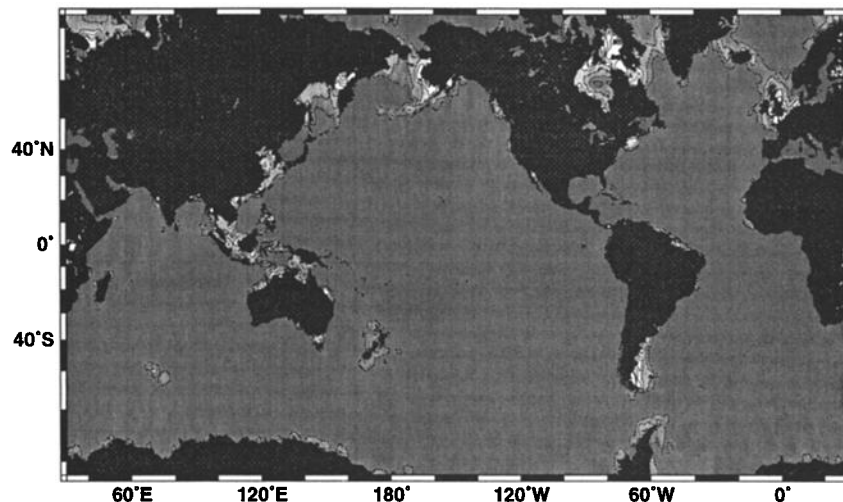


Figure 3. Absolute value of tide model slope [Eanes and Bettadpur, 1995]. Contours are at 0.5, 1, 2, 3, 4, and 5 μrad . One μrad of tidal slope error will map into ~ 1 mGal of gravity anomaly error. Tide models are most important on some shallow continental margins.

ocean tide model V3.0 [Bettadpur and Eanes, 1994; Eanes and Bettadpur, 1995] is superior to the tides supplied with either the Geosat GDRs or the ERS 1 OPR. Figure 3 shows the rms of the slope of the CSR V3.0 tide correction for a 35-day repeat cycle of ERS 1. Tidal slope corrections are usually small over the deep ocean but can be up to 6 μrad over some of the shallow continental margins. Previous versions of the global gravity grid did not incorporate this tide model correction and suffered from track line noise on the shallow areas surrounding Great Britain as well as on the Falkland Plateau; the CSR V3.0 tide model vastly improves the gravity field recovery in these and other areas.

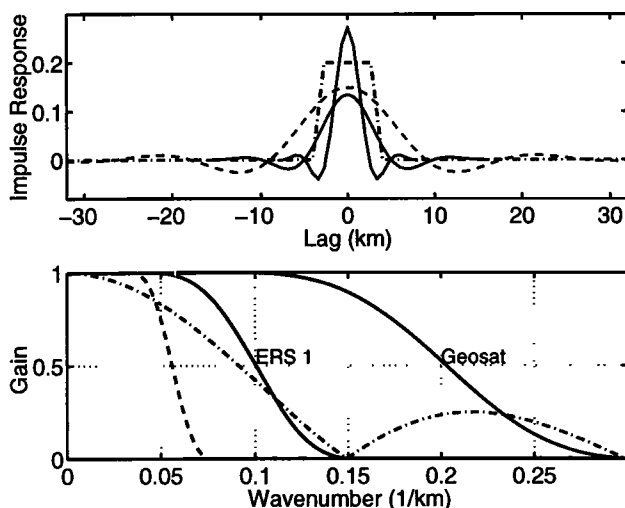


Figure 4. Prestack filters used on ERS 1 and Geosat altimeter data (solid). The poststack filter (dashed) is applied to all stacked and nonstacked profiles prior to gridding and has a 0.5 gain at a wavelength of 18 km. The 1-Hz boxcar filter (dashed-dot) is not suitable for resolving wavelengths shorter than about 30 km because of the large-amplitude sidelobes and slow roll-off. Filters were designed using the Remez routine in Matlab™ software. The routine is based on the Parks-McClellan finite impulse response filter design.

After editing and application of corrections, the data are broken into passes whenever a time gap exceeds 2 s (~ 14 km) or there is a change in pass orientation (e.g., from ascending to descending). The passes are low-pass filtered to suppress altimeter noise having wavelengths shorter than 5 km for Geosat and 10 km for ERS 1 as shown in Figure 4 (solid curves) and the filtered heights are subsampled at 5 Hz. Note that the 1-Hz boxcar filter (dashed-dot curves) followed by a 1-Hz decimation (i.e., the normal 1-Hz data supplied on both the GDR and OPR) will cause the sinc function sidelobes to fold from wavenumbers greater than 0.075 (13.4 km wavelength) to much longer wavelengths so that there is more than 20% aliasing at 20 km wavelength; thus a boxcar filter should not be used and the sampling rate should be greater than 2 Hz and preferably 5 Hz to retain all signals with wavelengths greater than 20 km.

The final and perhaps most important step in the preprocessing is to differentiate continuous profiles along track with respect to time. As shown in previous studies [e.g., Sandwell and Zhang, 1989], this suppresses long-wavelength errors and reference frame shifts so data adjustments are unnecessary. For simplicity, and to retain the ability to integrate the profiles, a first difference is used for the slope estimates. For example, the difference in height between points 1 and 2 is divided by their time difference and the slope is stored in location 1. This introduces a 1/2 phase shift (670 m) that is removed later with a second along-track filter.

Stacking

A study of the along-track resolution capabilities of stacked Geosat, ERS 1, and TOPEX altimeters was recently published by Yale *et al.* [1995] using the coherence method developed by Brammer [1979] and Marks and Sailor [1986]. Example profiles are shown in Figure 5 and an overview of the results is given in Table 1. All available data were loaded into three-dimensional files where repeat profiles were aligned along track. Outliers were detected by a comparison with the median of available cycles, and then the stack was computed as the average of the survivors. To determine the resolution improvement gained by stacking, the first half of available repeat profiles was averaged

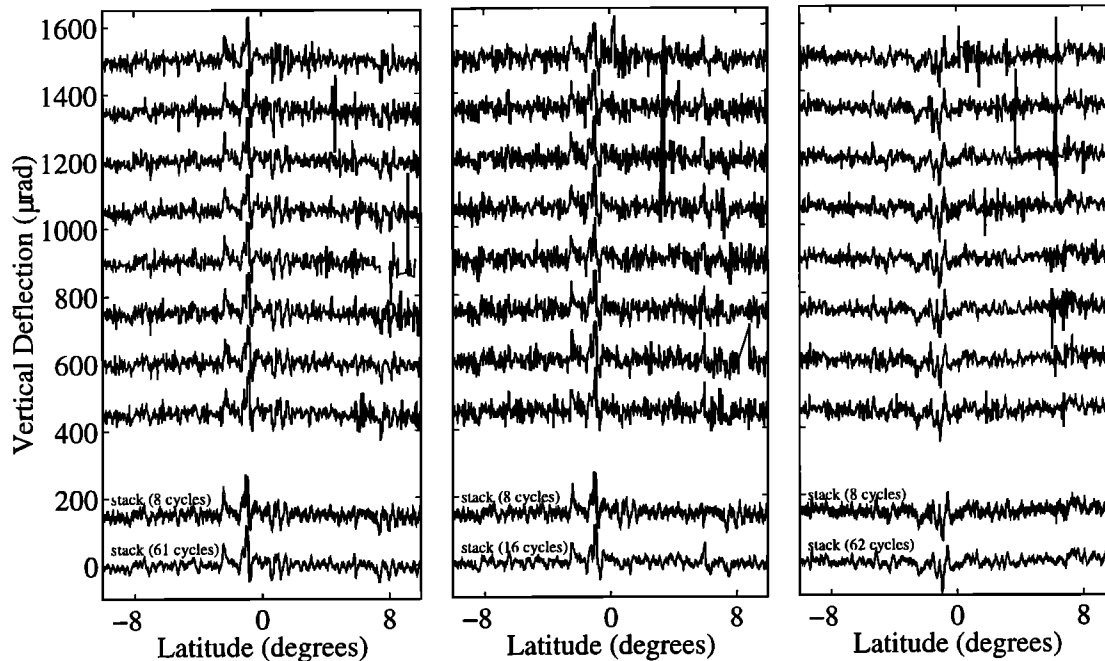


Figure 5. Individual and stacked vertical deflection profiles for a track crossing the Mid-Atlantic Ridge: (left) Geosat, (middle) ERS 1, (right) TOPEX. Only eight of the available cycles are shown for each satellite [from *Yale et al.*, 1995].

independently from the second half prior to the coherence analysis. Two areas were initially selected for coherence analysis: the equatorial Atlantic (Area 1 in Table 1), a region with high tectonic signal and low oceanographic noise; and the South Pacific (Area 2 in Table 1), a region with low tectonic signal and high oceanographic variability. In all cases, along-track resolution is better in the equatorial Atlantic than in the South Pacific; Geosat and TOPEX data resolve shorter wavelengths than ERS 1. Global maps of along-track resolution show considerable geographic variation. On average globally, the along-track resolution (0.5 coherence) of Geosat and TOPEX stacks are approximately the same (24 km), while the resolution of ERS 1 stacks are slightly worse (30 km). However, when equal numbers of repeat cycles are stacked, all three altimeters have about the same resolution limit of 28-30 km. The resolution estimates show that the shortest wavelength recoverable in the gravity field from satellite altimetry is about 20 km. Later, we apply an along-track filter to all of the profile data with a 0.5 gain at a wavelength of 18 km (Figure 4, dashed curves). Then after the north and east vertical deflection grids are created, they are low-pass filtered in two-dimensions with a filter having a 0.5 gain at 19 km.

Gridding: Accumulation, Interpolation, and Gravity Conversion

Our recipe for construction of gridded gravity anomalies from altimeter profiles works best when the track spacing is less than the along-track resolution of the altimeter data. The method was designed to accommodate large radial orbit error, long-wavelength tide model error, and shifts in reference associated with different tracking networks. In addition, it can accommodate data with differing accuracy, resolution, and pass orientation (Appendix B and Figure 6). Finally, the algorithm is fast enough so the entire world can be gridded on a workstation in a reasonable time (~2 days) (206 million observations and 68 million grid cells). We start with along-track slope estimates that were preprocessed and stacked as described above. The goal is to produce north and east vertical deflection grids that are consistent with the original observations to within their assigned noise level and where unconstrained cells reflect nearby values. The basic steps are (Figure 7) the following.

1. Edit nonstacked data by comparing the height value (i.e., integrated slope) with a Gaussian-filtered prediction from the surrounding points (0.5 gain at 36 km). If the suspect height

Table 1. Summary of Along-Track Resolution Estimates

	Area 1			Area 2			Global Average		
	Cycle	Stack 8	Stack 31	Cycle	Stack 8	Stack 31	Cycle	Stack 8	Stack 31
Geosat	33	26	20	52	38	27	38	29	24
ERS 1	38	26	-	50	33	-	43	30	-
TOPEX	34	24	19	43	31	23	37	28	22

Units in kilometers

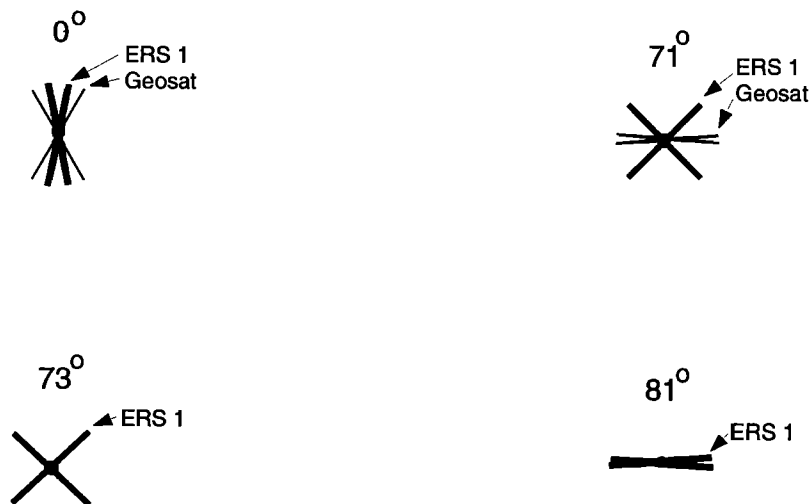
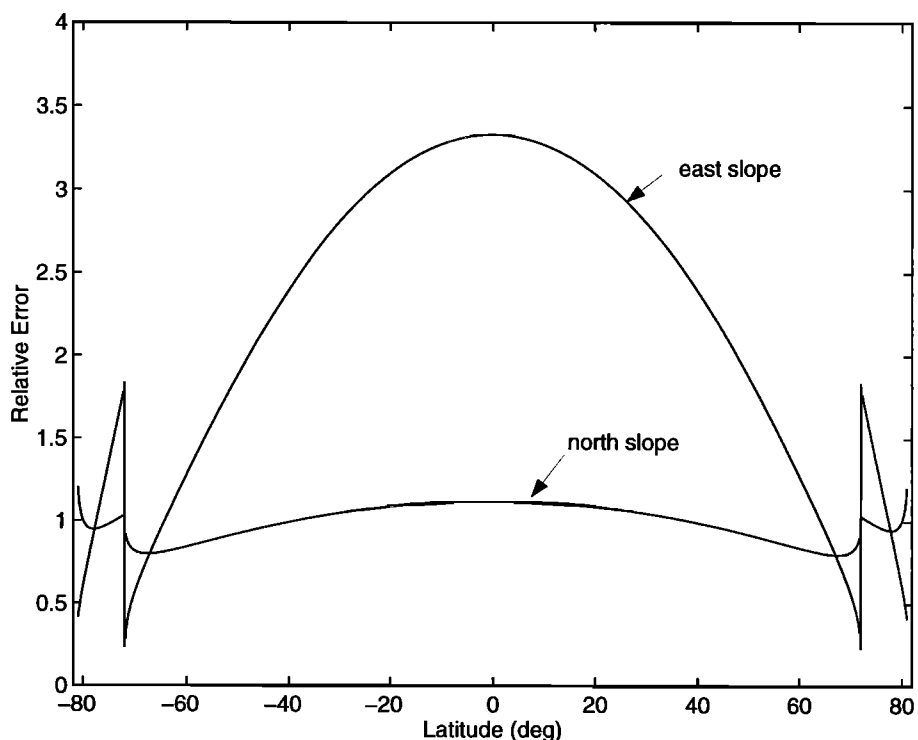


Figure 6. Propagation of along-track vertical deflection errors from dense Geosat and ERS 1 profiles into north and east components of vertical deflection. At the equator, satellite tracks run mainly N-S so the E-W component of vertical deflection is more poorly determined than the N-S component. This covariance information is used in both the blending during the iteration (Figure 7) and the filtering following the iteration (Figure 8).

estimate differed by more than 0.3 m from the prediction then that point was edited and the slope profile was recomputed.

2. Filter all of the along-track data with the same filter (0.5 gain at 18 km wavelength, Figure 4, dashed curves) to ensure a common bandwidth. The cutoff wavelength is based on the coherence analysis of *Yale et al.* [1995] which shows that the shortest possible wavelength resolvable is about 20 km. These two editing/filtering steps were not executed in the version 6.2 gravity field which resulted in a very noisy gravity model.

3. Remove from the profiles a reference geoid model based on JGM-3 [*Nerem et al.*, 1994] to degree 70 where coefficients are cosine tapered between degrees 50 and 70. This same field is restored later on; the reference field is removed so the vertical deflection to gravity anomaly conversion can be accurately performed with a flat-Earth approximation.

4. Bin data on an equidimensional Mercator grid with cell dimensions of 2 min in longitude and $\cos(\theta) \times 2$ min in latitude. The world is divided into 54 overlapping areas that are 1440 cells

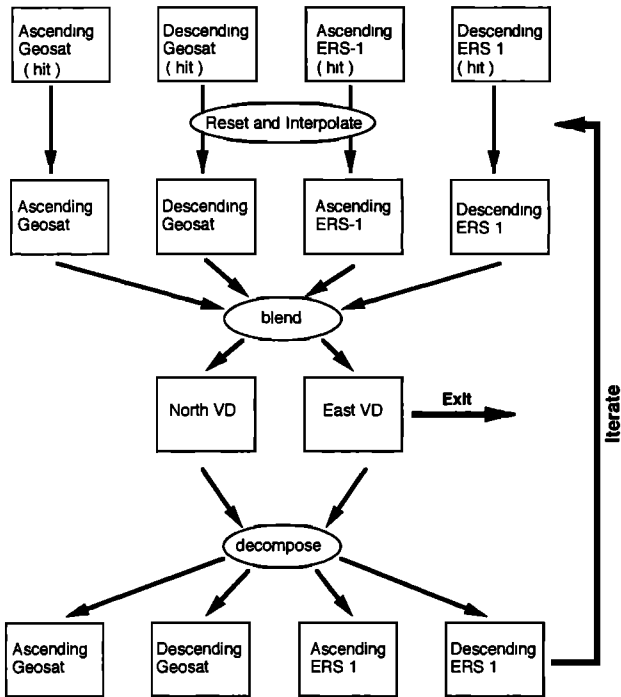


Figure 7. Flow diagram for constructing north and east grids of vertical deflection from ascending and descending along-track slope profiles. Iteration provides a communication among the diverse data sets [Menke, 1991].

wide (48°) and 1296 cells tall, so there is about 400 km of overlap on the perimeters. The areas are large enough so that the longest wavelength signal remaining in the residual profiles (~800 km) is less than the area dimension (> 2000 km). Data with common pass orientation are binned into these grid cells; unconstrained cells are left with an empty flag. Binning is done using the median value within the bin, and stacked profiles are counted 5 times so they will dominate the median.

5. Fill empty cells with reasonable values for the first iteration using a weighted average of surrounding data based on an $(\alpha + r)^{-3}$ weight function where α sets the width of the kernel and r is distance.

6. Blend pass-oriented grids using equation (B8) to form grids of north and east vertical deflection. Note that each data type is assigned a different weight according to expected noise level (ERS 1 noise = 1.41 x Geosat noise). Also note that the blending operation accounts for the pass orientation as illustrated in Figure 6.

7. Decompose the north and east grids into the original pass-oriented grids using equations (B1) and (B2).

8. Reset bins constrained by along-track slope observations to their original values unless they deviate from prediction by more than a threshold (15 μ rad, Geosat; 21 μ rad, ERS 1) in which case, edit the bin. Use biharmonic operator [Briggs, 1974; Smith and Wessel, 1990] to interpolate empty cells and go to step 6:

$$z_{0,0} = \frac{2}{5} (z_{1,0} + z_{0,1} + z_{-1,0} + z_{0,-1}) - \frac{1}{10} (z_{1,1} + z_{1,-1} + z_{-1,1} + z_{-1,-1}) - \frac{1}{20} (z_{0,2} + z_{2,0} + z_{-2,0} + z_{0,-2}) \quad (1)$$

where $z_{0,0}$ is the interpolated value based on the surrounding values z_{ij} . Steps (6) through (8) are repeated (Figure 7) until the values of unconstrained grid cells converge and the interpolated grids vary smoothly to zero in continental areas. Exit from the iteration after step (6).

9. The final step is to apply an isotropic, low-pass, convolution filter $[kei(\sqrt{2}r/\alpha)]$ to the north and east grids of vertical deflection. The filter width α is proportional to the fourth root of the relative error shown in Figure 6 in an attempt to equalize the noise level between the north and east slope grids. The exponential upward continuation model predicts that halving the error increases the resolution by $\sqrt{2}$. An additional $\sqrt{2}$ resolution is gained by averaging twice the amount of data. This is an arm-waving argument for using the fourth root of the relative error as the filter radius. In practice, the fourth-root model was found to work best. The wavelength at which the isotropic filter attenuates the signal by 0.5 is shown in Figure 8. For example, at the equator the ERS 1 and Geosat tracks provide relatively poor control on the east component so the 0.5-gain wavelength is 26 km while the 0.5 gain for the north component is 20 km.

After generating grids of north and east vertical deflection, various other derivatives of the gravitational potential can be computed. In all cases one should restore the appropriate derivatives of the spherical harmonic reference model that was removed in step 3. For example, the vertical gravity gradient is the sum of the x derivative of the east vertical deflection component and the y derivative of the north component – (equation (A6)) (Figure 2). The gravity anomaly is computed using (A10). The accuracy of this flat-Earth approximation is related to the cutoff wavelength of the spherical harmonic model removed (800 km for complete removal at degree 50). This requires Fourier transformation of each vertical deflection grid, combination in the wavenumber domain, and inverse Fourier transformation of the sum. If the grid pixels are equidimensional, then the transformation from vertical deflection to gravity largely avoids latitude-dependent length-scale problems [Haxby and Hayes, 1991]. For example, the operator on the Fourier transform of the east component of vertical deflection is $k_x/|k|$, so the length scale largely cancels. Maximum error introduced by this approximation will correspond to the change in length scale that

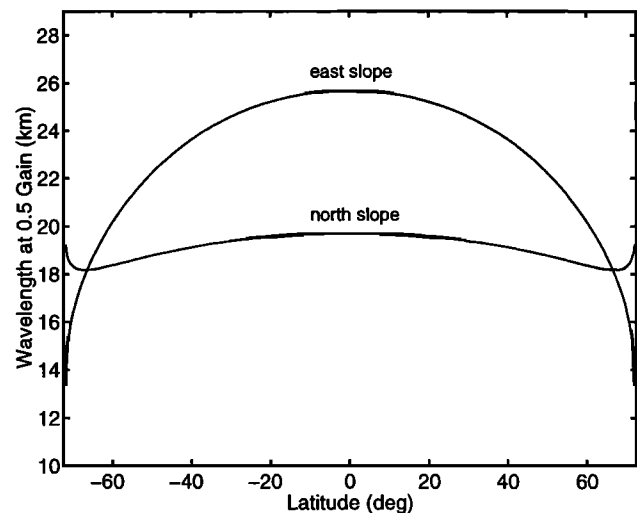


Figure 8. Cutoff wavelength (0.5 gain) of isotropic kei filter used to equalize the noise level in the north and east vertical deflection grids.

occurs over a latitude range corresponding to about 400 km of distance. At the equator this change is less than 0.2%, while at 70°N this change is 6%. We expect that the actual errors are smaller than this because most of the contribution to the gravity anomaly will be nearby. The error due to this "flat Earth" approximation is reduced as the spherical harmonic degree of the reference model is increased as long as there are no errors in the reference model [Haxby and Hayes, 1991]. Also note that to safely avoid edge effects the dimensions of the vertical deflection grids must be several times larger than the longest wavelength remaining in the residual data. The final step in the gravity computation is to restore the gravity anomaly corresponding to the spherical harmonic model removed in step 3.

Accuracy and Resolution

The accuracy and resolution of gravity grids constructed using a similar approach were recently established through a comparison with accurate shipboard gravity measurements [Neumann *et al.*, 1993]. For a small region along the southern Mid-Atlantic Ridge where there is a dense shipboard survey and large gravity anomalies (140 mGal total variation), the rms difference is 7-8 mGal when only Geosat/GM data are used. Marks [1996] has recently compared seven well-navigated shipboard profiles with this latest version of our grid as well as a Geosat-only grid [Marks *et al.*, 1993] to assess the resolution of the satellite-derived gravity and improvement gained by adding ERS 1 altimeter data. She found agreement (0.5 coherence) to wavelengths of 23-30 km for this Geosat/ERS 1 grid and 26-30 km for the Geosat-only grid; rms differences ranged from 3 to 9 mGal. This resolution analysis compares well with estimates derived from repeat track analysis [Yale *et al.*, 1995] and further justifies the use of along-track and two-dimensional filters to cut (0.5 gain) wavelengths shorter than 20 km.

We also compare shipboard gravity profiles with the satellite-derived gravity grid and find that individual ship profiles show

rms differences of 3-6 mGal depending on proximity to a stacked altimeter profile. The first two examples are from ship profiles that follow the track line of two Geosat/ERM profiles in the South Atlantic [Jung and Vogt, 1992]. Along the Conrad 2802 profile, the ship track deviates from the Geosat track line at -20.5° latitude to avoid a small island. The mean difference between the Geosat-derived gravity and the shipboard gravity is -0.57 mGal, and the rms difference is 2.76 mGal when the island/seamount data are omitted (Figure 9a). The difference at the crest of the seamount is about 50 mGal, which is probably due to lack of short-wavelength components in the satellite-derived gravity field. The second example (eastern South Atlantic) crosses the Walvis ridge and has a similar rms misfit (3.03 mGal) but a large mean difference (16.82 mGal) (Figure 9b). This large mean difference probably reflects an error in the ship gravity measurement at the tie point, or perhaps no tie point correction was made. It should be noted that a 3-mGal error corresponds to a relative height accuracy of only 15 mm over a distance of 5 km (i.e., 1/4 of the resolution wavelength). Considering that typical surface wave heights are a meter or more tall, this is a remarkable achievement. When repeating profiles are stacked, the vertical deflection error decreases as the square root of the number of profiles used in the stack [Yale *et al.*, 1995].

To establish the accuracy of the satellite-derived grid in areas away from repeat altimeter profiles, we selected data from two well-navigated Conrad cruises on the western flank of the northern Mid-Atlantic Ridge (Figure 10a). Note this is the same ship, gravimeter, and navigation system that was used for the South Atlantic comparison (Figure 9); thus differences will reflect proximity to a stacked Geosat/ERM profile. All three cruises stop in the Azores where we assume the tie point correction was established. Three segments were tested, c2912 outbound from Spain to the Mid-Atlantic Ridge (Figure 10b, mean 13.01 mGal, rms 5.80 mGal), c2912 from Mid-Atlantic Ridge to the Azores (Figure 9c, mean 13.92 mGal, rms 5.84 mGal), and c3001 from the Azores to the Mid-Atlantic Ridge (Figure 9c, mean 12.43

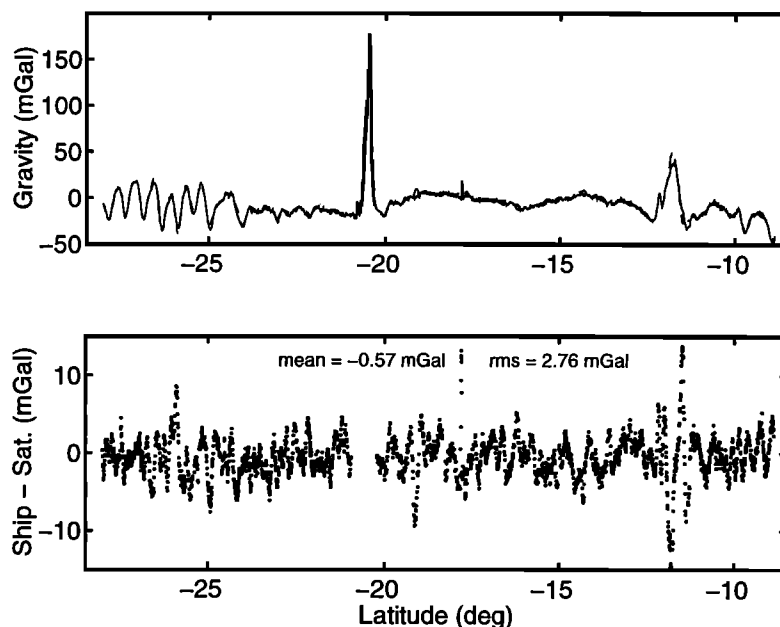


Figure 9a. Comparison between a shipboard gravity profile Conrad 2802 in the western South Atlantic (solid [see Jung and Vogt, 1992]) with gravity profile along a track corresponding to a 62-fold stack of Geosat altimeter profiles (dashed). The difference was not computed at -21.5°S latitude where the ship track deviates from the satellite track to avoid an island.

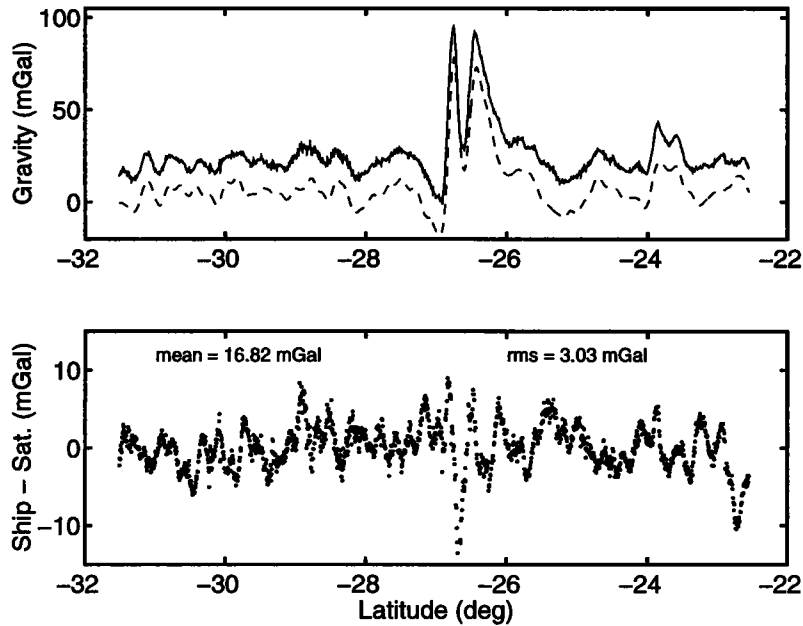


Figure 9b. Similar comparison for Conrad 2711 along Geosat/ERM suborbital track in the eastern South Atlantic.

mGal, rms 6.70 mGal). Note that for a short distance the ship tracks are nearly coincident and there is a good match among all six profiles (Figure 10c). From these comparisons we conclude the following: (1) Away from a stacked Geosat/ERM profile the accuracy of the satellite-derived gravity field degrades to 4-7 mGal. Given a typical combined Geosat/ERS 1 track spacing of about 2.5 km and a 1/2 wavelength resolution of 10 km there is a redundancy of about four tracks over most of the grid. This can be compared to a typical redundancy of 40 along the stacked Geosat/ERM profile [Yale *et al.*, 1995]. Thus a 3.2 times improvement in accuracy near the stacked profile is to be expected but only a 2 times improvement is observed; of course ocean depth and typical sea state are other major considerations. (2) The good match between the satellite-derived gravity and the shipboard gravity over the sharp 350-mGal anomaly at a longitude of 344° (Figure 10b) demonstrates there are no major problems with either the dynamic range of the altimeter or the data processing. (3) The systematic disagreement in mean level

of 13 mGal between the cruises c2912 and c3001 suggests that there is a 13-mGal error in a common tie point. The implication is that one could correct the DC level of all shipboard gravity profiles through comparison with the gravity grid [Wessel and Watts, 1988; Smith and Sandwell, 1995]. Moreover, instrument drift and other more subtle errors such as navigation-induced error could be corrected.

Based on these ground truth analyses, one could expect perhaps a factor of 2 improvement in the accuracy of the satellite-derived gravity field by collecting at least 4 times more data. The Geosat/GM and ERS 1/GM missions reflect 2.5 years of data, so a 10-year dedicated mapping mission would be needed. In the deep oceans the upward continuation causes the amplitudes of the anomalies to decrease exponentially with decreasing wavelength, so a factor of 2 improvement in accuracy would only yield a 1.4 increase in resolution to about 18 km. Such a resolution increase would be geophysically significant, especially for hydrocarbon exploration where the current satellite-derived gravity fields are

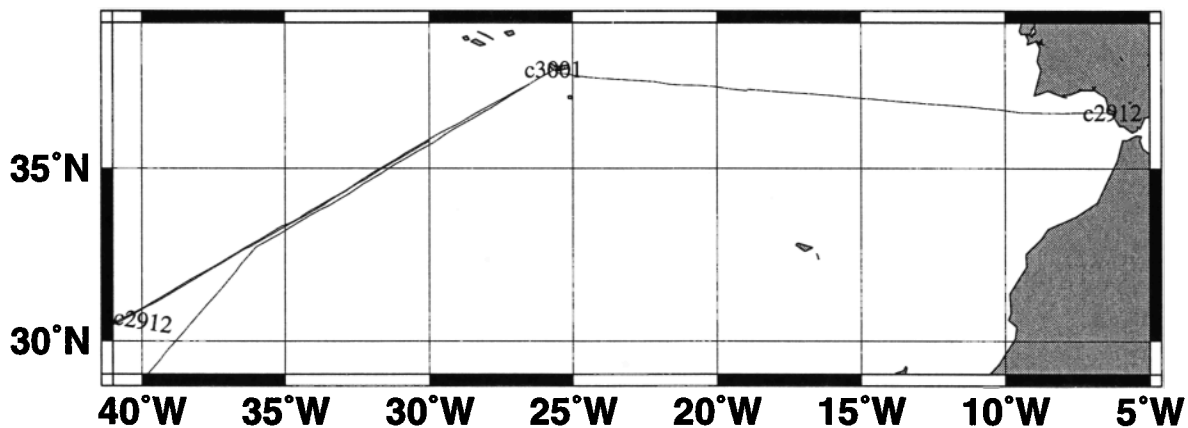


Figure 10a. Comparison between satellite-derived gravity and gravity along random ship tracks. (a) Location of Conrad 2912 Spain to Azores to Mid-Atlantic Ridge and repeating track back to Azores. Location of Conrad 3001 from Azores to Mid-Atlantic Ridge along same track line.

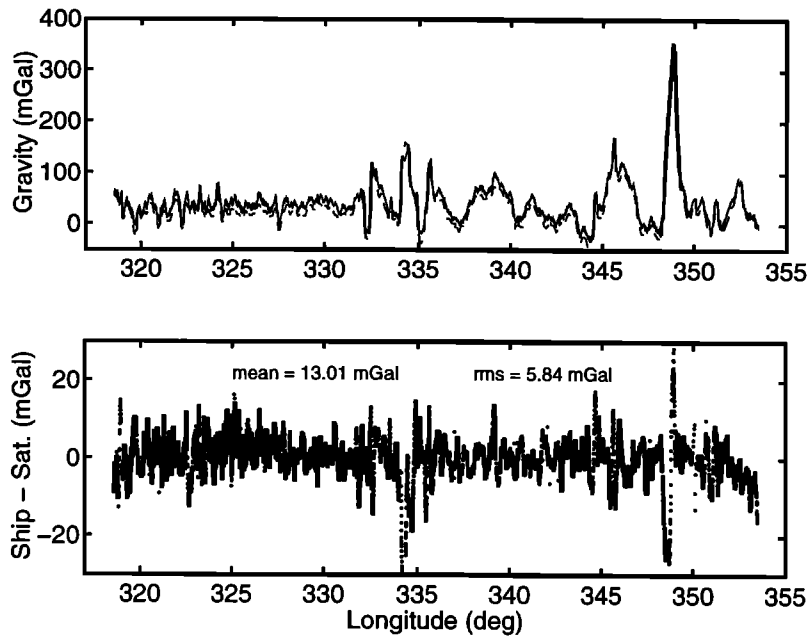


Figure 10b. Comparison along outbound track of C2912, outbound.

marginally useful. Perhaps a new technology such as a scanning laser altimeter or a multibeam radar altimeter could provide this enhanced gravity field in a shorter time period.

Applications

Navigation

The Geosat data were collected by the U.S. Navy to fulfill their navigational and mapping requirements. Consider measuring accelerations in a moving submarine or aircraft in order to

determine your position as a function of time. (Of course, your starting position and velocity must also be known.) If the windows of your vehicle are closed, a true acceleration cannot be distinguished from a variation in the pull of gravity. Thus the gravity data are needed for correction of inertial navigation/guidance systems. The military applications are obvious and provided the rationale for the \$80 million cost of the Geosat mission as well as the classification of these data, especially during the cold war when nuclear submarines were more active than they are today. On the commercial side, Honeywell Inc. is using these data to update their inertial navigation systems aboard

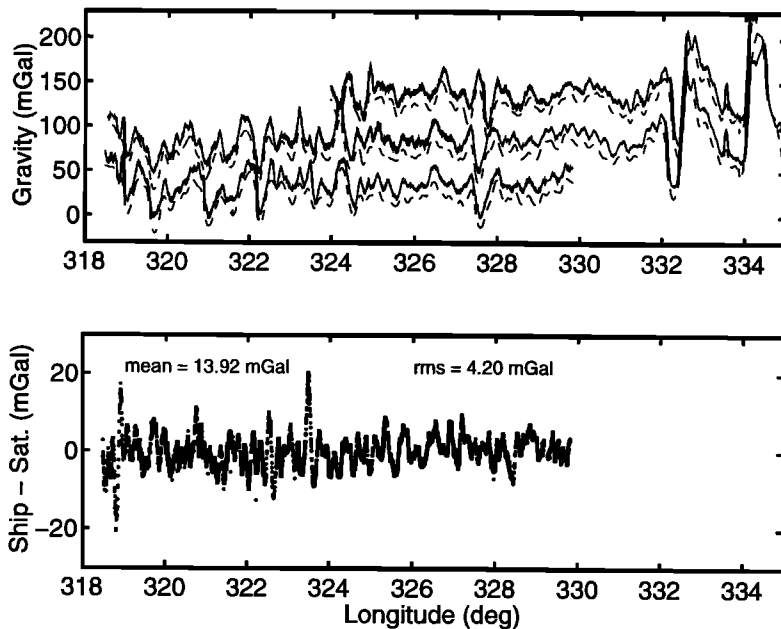


Figure 10c. Comparison where three ship tracks are nearly coincident (top, c3001; middle, c2912 outbound; bottom, c2912 inbound).

aircraft. In particular, when this correction is not applied, they have found large navigational errors along Pacific Ocean flight paths which follow the major ocean trenches (K. Vanderwerf, Honeywell Inc., Coon Rapids, Minnesota, personal communication, 1995).

Prediction of Seafloor Depth

We are using these dense satellite altimeter measurements in combination with sparse measurements of seafloor depth to construct a uniform resolution map of the seafloor topography [Smith and Sandwell, 1994]. These maps do not have sufficient accuracy and resolution to be used to assess navigational hazards, but they are useful for such diverse applications as locating the obstructions/constrictions to the major ocean currents and locating shallow seamounts where fish and lobster may be abundant. An intermediate step in the depth prediction process determines the correlation between gravity and depth and a number inversely proportional to the seafloor density contrast; these parameters may be used as proxies for sediment thickness.

On a broad scale the topography of the ocean floor reflects the cooling and subsidence of the plates as they move away from the spreading center. While this process is fairly well understood, there are interruptions in this normal subsidence caused by mantle plumes and other types of solid-state convection in the mantle of the Earth.

Planning Shipboard Surveys

The satellite-derived gravity grids reveal all of the major structures of the ocean floor having widths greater than 10-15 km. This resolution matches the total swath width of the much higher resolution (100 m) multibeam mapping system on a ship so the gravity maps are the perfect reconnaissance tool for planning the more detailed shipboard surveys. Scientists aboard research vessels use the gravity grids along with other measurements to optimize their survey strategy; in many cases this is done in real time. The cost to operate a research vessel is typically \$20,000 per day, so these gravity data have become an essential item.

Plate Tectonics

These satellite altimeter data provide an important and definitive confirmation of the theory of plate tectonics. Indeed, almost everything apparent in the marine gravity field was created by the formation and motion of the plates. Spreading ridges are characterized by an orthogonal pattern of ridges and transform faults. The scar produced in the active transform valley is carried by seafloor spreading out onto older seafloor, leaving evidence of the past plate motions. The Indian Ocean triple junction (27°S latitude, 70°E longitude) is a textbook example of seafloor spreading. The satellite-derived gravity field shows the intersection of the three spreading ridges as described by plate tectonic theory. The theory predicts that the ridges would intersect at 120° angles if the three ridges were spreading at exactly the same rate. In this case, one can measure the intersection angles and infer the relative spreading rates of each ridge.

Plates are created at spreading ridges and destroyed (subducted) at the deep ocean trenches. All of the major ocean trenches are evident in the gravity map as linear troughs. The deep ocean basins away from the trenches are characterized by fracture zone gravity signatures inherited at the spreading ridge axis. This pattern is sometimes overprinted by linear volcanic

chains which are believed to be formed as the plate moves over a stationary mantle plume. The hot plume head melts the mantle rocks which erupt on the surface as a hot spot. Because all of these major features are evident in the gravity maps, the geologic history of the ocean basins can now be established in greater detail.

Undersea Volcanoes

The global gravity grids reveal all volcanoes on the seafloor greater than about 1000 m tall. Approximately 30-50% of these volcanoes were not charted previously. One of the more important aspects of these new data will be to locate all of these volcanoes and identify spatial patterns that may help determine how they formed. Many volcanoes appear in chains, perhaps associated with mantle plumes, but there are many more that do not fit this simple model. Moreover, numerous undersea volcanoes are long linear ridges with aspect ratios of 20 or more. These features suggest that the plates are not exactly rigid as predicted by the simple plate tectonic theory. Using these data, we are exploring the internal deformations of the plates, especially outboard of trenches where the forces generated by the slab-pull force of the subducted plates are greatest.

Petroleum Exploration

All of the major petroleum exploration companies use satellite altimeter gravity data from Geosat and ERS 1 to locate offshore sedimentary basins in remote areas. This information is combined with other reconnaissance survey information to determine where to collect or purchase multichannel seismic survey data. Currently, the regions of most intense exploration interest are the continental shelves of Australia and the former Soviet Union; recently, companies have expressed interest in the Caspian Sea. Developments in offshore drilling technology now make it economical to recover oil from continental slope areas in water once thought prohibitively deep.

While we are not directly involved in this activity, we fill data requests from many large exploration companies including Unocal, Amoco, Exxon, Arco, Mobil, Texaco, Shell, Conoco, and British Petroleum, as well as many smaller exploration companies.

Lithospheric Structure

There are numerous other scientific applications that cannot be described in a short report. One of the traditional uses of marine gravity measurements is to estimate the thickness of the elastic portion of the tectonic plates [Watts, 1979]. When a volcano forms on the ocean floor it imparts a large downward load on the plate causing it to deform. This deformation appears in the gravity field as a donut-shaped gravity low surrounding the gravity high associated with the volcano itself. By measuring the amplitude and width of the gravity low and relating this to the size of the volcano as measured by a ship with an echo sounder, one can establish the thickness and strength of the elastic plate. The new satellite-derived gravity data enable researchers to perform this type of analysis everywhere in the oceans. Thus scientists can now probe the outermost part of the Earth using these and other methods.

A gridded file of gravity anomalies (version 7.2) is available by anonymous ftp (baltica.ucsd.edu). A large-format, laminated poster is available from the Scripps Institution of Oceanography Geological Data Center. Also visit our web site http://topex.ucsd.edu/mar_grav.html.

Appendix A: Geoid Height, Vertical Deflection, Gravity Gradient, and Gravity Anomaly

The geoid height $N(\mathbf{x})$ and other measurable quantities such as gravity anomaly $\Delta g(\mathbf{x})$ are related to the gravitational potential $V(\mathbf{x}, z)$ [Heiskanen and Moritz, 1967]. We assume that all of these quantities are deviations from a spherical harmonic reference Earth model so a flat-Earth approximation can be used for the gravity computation (A10). In the following equations the bold \mathbf{x} denotes the coordinate (x, y) ; similarly \mathbf{k} denotes (k_x, k_y) where $k_x = 1/\lambda_x$, where λ_x is wavelength. To a first approximation, the geoid height is related to the gravitational potential by Brun's formula,

$$N(\mathbf{x}) \equiv \frac{1}{g_o} V(\mathbf{x}, 0) \quad (\text{A1})$$

where g_o is the average acceleration of gravity (9.81 m s^{-2}). The gravity anomaly is the vertical derivative of the potential

$$\Delta g(\mathbf{x}) = - \frac{\partial V(\mathbf{x}, 0)}{\partial z} \quad (\text{A2})$$

the east component of vertical deflection is the slope of the geoid in the x direction

$$\eta(\mathbf{x}) \equiv - \frac{\partial N}{\partial x} \equiv - \frac{1}{g_o} \frac{\partial V}{\partial x} \quad (\text{A3})$$

and the north component of vertical deflection is the slope of the geoid in the y direction.

$$\xi(\mathbf{x}) \equiv - \frac{\partial N}{\partial y} \equiv - \frac{1}{g_o} \frac{\partial V}{\partial y} \quad (\text{A4})$$

These quantities are related to one another through Laplace's equation

$$\frac{\partial^2 V}{\partial x^2} + \frac{\partial^2 V}{\partial y^2} + \frac{\partial^2 V}{\partial z^2} = 0. \quad (\text{A5})$$

Substitution of (A2), (A3), and (A4) into Laplace's equation (A5) yields a relationship between the vertical gravity gradient and the sum of the x and y derivatives of the east and north vertical deflection

$$\frac{\partial \Delta g}{\partial z} = -g_o \left(\frac{\partial \eta}{\partial x} + \frac{\partial \xi}{\partial y} \right) \quad (\text{A6})$$

This expression is used to compute vertical gravity gradient (Figure 2) from grids of east and north vertical deflection [Rummel and Haagmans, 1990]. Note that this is a local

computation which does not involve spherical harmonics or Fourier transforms. Indeed, given two orthogonal satellite altimeter profiles, the vertical gravity gradient at their intersection point is the sum of the curvatures of each profile times the average acceleration of gravity. The simplicity of this calculation is particularly desirable for computing the gravity gradient near coastlines where the altimeter profiles terminate; the calculation of the vertical gravity gradient from (A6) has no edge effect, while the Fourier computation of the gravity field can have a significant edge effect.

In contrast to the simple formulation of the gravity gradient, computation of the gravity anomaly is much more difficult and error prone. Following Haxby *et al.* [1983], the differential equation (A5) is reduced to an algebraic equation by Fourier transformation. The forward and inverse Fourier transforms are defined as

$$\begin{aligned} F(\mathbf{k}) &= \int_{-\infty}^{\infty} \int_{-\infty}^{\infty} f(\mathbf{x}) e^{-i2\pi(\mathbf{k}\cdot\mathbf{x})} d^2\mathbf{x} \\ f(\mathbf{x}) &= \int_{-\infty}^{\infty} \int_{-\infty}^{\infty} F(\mathbf{k}) e^{i2\pi(\mathbf{k}\cdot\mathbf{x})} d^2\mathbf{k}. \end{aligned} \quad (\text{A7})$$

The Fourier transform of (A6) is

$$\frac{\partial \Delta g(\mathbf{k}, z)}{\partial z} = -i2\pi g_o [k_x \eta(\mathbf{k}) + k_y \xi(\mathbf{k})]. \quad (\text{A8})$$

From the solution to Laplace's equation in the wavenumber domain the upward continuation formula relates the gravity anomaly at the surface of the Earth to the gravity anomaly at some elevation z .

$$\Delta g(\mathbf{k}, z) = \Delta g(\mathbf{k}, 0) \exp(-2\pi|\mathbf{k}|z) \quad (\text{A9})$$

where $|\mathbf{k}| = \sqrt{k_x^2 + k_y^2}$. Taking the derivative of (A9) with respect to z and evaluating the result at $z = 0$, one arrives at an algebraic formula relating the Fourier transform of the gravity anomaly to the sum of the Fourier transforms of the two components of vertical deflection:

$$\Delta g(\mathbf{k}, 0) = \frac{ig_o}{|\mathbf{k}|} [k_x \eta(\mathbf{k}) + k_y \xi(\mathbf{k})]. \quad (\text{A10})$$

To compute gravity anomalies from a dense network of satellite altimeter profiles of geoid height, one constructs a grid of east η and north ξ vertical deflection (Appendix B). The grids are then Fourier transformed using a discrete approximation to (A7). Finally, one performs the multiplications given in (A10) and inverse Fourier transforms the result to obtain gravity anomaly. At this point one could also add the spherical harmonic gravity model back to the gridded gravity values in order to recover the long wavelength gravity field.

Appendix B: Vertical Deflections From Along-Track Slopes

To avoid any adjustment of the data, ascending and descending satellite altimeter profiles are first differentiated in the along-track

direction resulting in geoid slopes or along-track vertical deflections. These along-track vertical deflections are then combined to produce east η and north ξ components of vertical deflection [Sandwell, 1984]. Finally, the east and north vertical deflections are used to compute both gravity anomaly and vertical gravity gradient (Appendix A). The algorithm used for gridding the altimeter profiles is an iteration scheme that relies on rapid transformation from ascending/descending geoid slopes to north/east vertical deflection and vice versa. Consider for the moment the intersection point of an ascending and a descending satellite altimeter profile. The derivative of the geoid height N with respect to time t along the ascending profile is

$$\dot{N}_a \equiv \frac{\partial N_a}{\partial t} = \frac{\partial N}{\partial \theta} \dot{\theta}_a + \frac{\partial N}{\partial \phi} \dot{\phi}_a \quad (B1)$$

and along the descending profile is

$$\dot{N}_d = \frac{\partial N}{\partial \theta} \dot{\theta}_d + \frac{\partial N}{\partial \phi} \dot{\phi}_d \quad (B2)$$

where θ is geodetic latitude and ϕ is longitude. The functions $\dot{\theta}$ and $\dot{\phi}$ are the latitudinal and longitudinal components of the satellite ground track velocity (Appendix C). It is assumed that the satellite altimeter has a nearly circular orbit so that its velocity depends mainly on latitude; at the crossover point the following relationships are accurate to better than 0.1%.

$$\dot{\theta}_a = -\dot{\theta}_d \quad \dot{\phi}_a = \dot{\phi}_d \quad (B3)$$

(Analytic expressions for satellite velocities are given in Appendix C using orbit parameters in Table C1.) The geoid gradient is obtained by solving (B1) and (B2) using (B3).

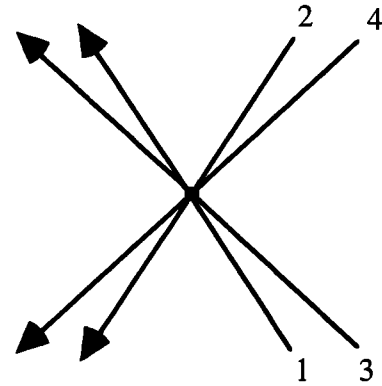
$$\frac{\partial N}{\partial \phi} = \frac{1}{2\dot{\phi}} (\dot{N}_a + \dot{N}_d) \quad (B4)$$

$$\frac{\partial N}{\partial \theta} = \frac{1}{2|\dot{\theta}|} (\dot{N}_a - \dot{N}_d) \quad (B5)$$

It is evident from this formulation that there are latitudes where either the east or north component of geoid slope may be poorly determined. For example, at $\pm 72^\circ$ latitude the Seasat and Geosat altimeters reach their turning points where the latitudinal velocity $\dot{\theta}$ goes to zero and thus (B5) becomes singular. In the absence of noise this is not a problem because the ascending and descending profiles are nearly parallel so that their difference goes to zero at the same rate that the latitudinal velocity goes to zero. Of course, in practice, altimeter profiles contain noise, so that the north component of geoid slope will have a signal-to-noise ratio that decreases near $\pm 72^\circ$ latitude. Similarly, for an altimeter in a near polar orbit the ascending and descending profiles are nearly antiparallel at the low latitudes; the east component of geoid slope is poorly determined and the north component is well determined. The optimal situation occurs when the tracks are

nearly perpendicular so that the east and north components of geoid slope have the same signal-to-noise ratio.

When two or more satellites with different orbital inclinations are available, the situation is slightly more complex but also more stable. Consider the intersection of four passes as shown in below.



The along-track derivative of each pass can be computed from the geoid gradient at the crossover point

$$\begin{bmatrix} \dot{N}_1 \\ \dot{N}_2 \\ \dot{N}_3 \\ \dot{N}_4 \end{bmatrix} = \begin{bmatrix} \dot{\theta}_1 & \dot{\phi}_1 \\ \dot{\theta}_2 & \dot{\phi}_2 \\ \dot{\theta}_3 & \dot{\phi}_3 \\ \dot{\theta}_4 & \dot{\phi}_4 \end{bmatrix} \begin{bmatrix} \frac{\partial N}{\partial \theta} \\ \frac{\partial N}{\partial \phi} \end{bmatrix} \quad (B6)$$

or in matrix notation

$$\dot{N} = \Theta \nabla N \quad (B7)$$

Since this is an overdetermined system, the four along-track slope measurements cannot be matched exactly unless the measurements are error free. In addition, an a priori estimate of the error in the along-track slope σ_j measurements can be used to weight each equation in (B6) (i.e., divide each of the four equations by σ_j). The least squares solution to (B7) is

$$\nabla N = (\Theta^t \Theta)^{-1} \Theta^t \dot{N} \quad (B8)$$

where t and -1 are the transpose and inverse operations, respectively. In this case a 2 by 4 system must be solved at each crossover point, although the method is easily extended to three or more satellites. Later we will assume that every grid cell corresponds to a crossover point of all the satellites considered, so this small system must be solved many times.

In addition to the estimates of geoid gradient, the covariances of these estimates are also obtained:

$$\begin{bmatrix} \sigma_{\theta\theta}^2 & \sigma_{\theta\phi}^2 \\ \sigma_{\phi\theta}^2 & \sigma_{\phi\phi}^2 \end{bmatrix} = (\Theta^t \Theta)^{-1} \quad (B9)$$

We use the covariance estimates to low-pass filter the north component of geoid slope differently from the east component

depending on latitude. An example of covariance estimates for a combination of Geosat and ERS 1 is shown in Figure 6 where the standard deviation of ERS 1 was set to 1.4 times the standard deviation of Geosat. Since Geosat and ERS 1 are high-inclination satellites, the estimated uncertainty of the east component is about 3 times greater than the estimated uncertainty of the north component at the equator. At higher latitudes of 60°-70° where the tracks are nearly perpendicular, the north and east components are equally well determined. At 72°N where the Geosat tracks run in a westerly direction, the uncertainty of the east component is low and the higher-inclination ERS 1 tracks prevent the estimate of the north component from becoming singular at 72°.

Finally, the east η and north ξ components of vertical deflection are related to the two geoid slopes [Heiskanen and Moritz, 1967] by

$$\eta = -\frac{1}{a \cos \theta} \frac{\partial N}{\partial \phi} \quad (\text{B10})$$

$$\xi = -\frac{1}{a} \frac{\partial N}{\partial \theta} \quad (\text{B11})$$

where a is the mean radius of the Earth.

Appendix C: Approximate Satellite Position and Velocity

The exact satellite ground track velocity could be calculated directly from the ground track profiles supplied with the satellite altimeter data records. However, later on we will need to evaluate (B1), (B2), and (B6) at grid cells that were not necessarily intersected by a satellite profile. Thus it is desirable to have accurate formulae for computing θ and $\dot{\phi}$ versus latitude. In addition, the accumulation of the along-track repeat profiles into the stack files require an approximate trajectory for the satellite. Thus we derive expressions for both the approximate position and velocity of a satellite in a circular orbit about an ellipsoidal Earth. The important parameters are the orbit frequency ω_s , the Earth rotation rate ω_e , the precession rate of the orbit plane about the Earth's spin axis ω_n , the inclination of the satellite orbit I , the flattening of the Earth f , the starting longitude of the satellite ϕ_0 , the geocentric latitude θ_c , and the geodetic latitude θ . Numerical values of the constant parameters are given in Table C1.

To attain the desired level of approximation, it is necessary to account for the flattening of the Earth when computing latitude

and latitudinal velocity. Assuming the Earth is an oblate ellipse with flattening f , the conversion from geocentric θ_c to geodetic latitude θ is

$$\tan \theta = (1 - f)^2 \tan \theta_c. \quad (\text{C1})$$

At the equator and at the poles, the two latitudes are equal, but at intermediate latitudes (e.g., 45°) they differ by up to 0.2°. The derivative of (C1) with respect to time provides the correction to the latitudinal velocity when converting from the geocentric system to the geodetic system.

$$\frac{\dot{\theta}}{\dot{\theta}_c} = (1 - f)^2 \frac{\cos^2 \theta}{\cos^2 \theta_c}. \quad (\text{C2})$$

Equations for the relative position of the satellite versus time were derived following Kaula [1966]. The basic problem is to map the position of a satellite in a circular orbit about the Earth into an Earth-fixed coordinate system. Let $t = 0$ be the time when the satellite orbit crosses the Earth's equatorial plane on an ascending pass at a longitude of ϕ_0 . To develop formulae, one first represents the position of the satellite in a Cartesian coordinate system \mathbf{q} where the q_x axis is the line connecting the center of the Earth and the ascending equator crossing. The q_z axis is perpendicular to the orbit plane and the q_y axis is orthogonal to the q_x and q_z axes. In this frame the q_x , q_y , and q_z positions are $\cos(\omega_s t)$, $\sin(\omega_s t)$, and 0, respectively. Next the satellite frame is rotated about the q_x axis by the inclination of the orbit plane relative to the Earth's equatorial plane I . A third rotation about the Earth's spin axis maps the satellite plane into an Earth-fixed system. This final rotation involves the rotation rate of the Earth relative to the precessing orbit plane $\omega_e' = \omega_e - \omega_n$. After performing the three rotations and transforming the results from Cartesian coordinates into spherical coordinates, one obtains expressions for the latitude and longitude versus time. The geocentric latitude is

$$\theta_c(t) = \sin^{-1} [\sin \omega_s t \sin I]. \quad (\text{C3})$$

This geocentric latitude is converted to geodetic latitude using equation (C1). In addition, (C3) can be inverted to yield the time since the equator crossing

$$t(\theta_c) = \omega_s^{-1} \sin^{-1} \left[\frac{\sin \theta_c}{\sin I} \right]. \quad (\text{C4})$$

Table C1. Orbit Geometric Parameters

Description	GEOS 3	Seasat	Geosat	TOPEX	ERS 1
ω_s orbit frequency, s^{-1}	1.0420×10^{-3}	1.0407×10^{-3}	1.0407×10^{-3}	9.3143×10^{-4}	1.0379×10^{-3}
ω_n precess frequency, s^{-1}	-4.143×10^{-7}	-6.743×10^{-5}	$(\omega_e - \omega_s) 17/244$	$(\omega_e - \omega_s) 10/127$	$(\omega_e - \omega_s) 35/501$
I inclination	114.980°	108.0584°	108.0584°	66.010°	98.5557°
ω_e Earth rotation frequency, s^{-1}	7.29212×10^{-5}				
f flattening	1/298.25				
a earth radius, m	6371000				
g_0 acceleration of gravity, $m s^{-2}$	9.81				

The cosine and sine of the longitude (relative to ϕ_0) at some later time are given by

$$\cos\phi(t) = \left[\frac{\cos\omega_e't \cos\omega_s't + \sin\omega_e't \sin\omega_s't \cos I}{\cos\theta_c(t)} \right] \quad (C5)$$

and

$$\sin\phi(t) = \left[\frac{-\sin\omega_e't \cos\omega_s't + \cos\omega_e't \sin\omega_s't \cos I}{\cos\theta_c(t)} \right]. \quad (C6)$$

By combining these two expressions, the longitude at a later time is

$$\phi(t) = \tan^{-1} \left[\frac{-\sin\omega_e't \cos\omega_s't + \cos\omega_e't \sin\omega_s't \cos I}{\cos\omega_e't \cos\omega_s't + \sin\omega_e't \sin\omega_s't \cos I} \right] + \phi_0 \quad (C7)$$

Given these equations for position versus time, one can derive expressions for the latitudinal and longitudinal components of the satellite velocity versus latitude. The latitudinal velocity is obtained by differentiating (C3) with respect to time and using (C4) to relate velocity to latitude instead of time. The result is

$$\dot{\theta}_c(\theta_c) = \omega_s \left[1 - \frac{\cos^2 I}{\cos^2 \theta_c} \right]^{1/2}. \quad (C8)$$

Of course, the sign of the velocity will depend on whether the satellite profile is ascending (+) or descending (-). To convert from geocentric velocity to geodetic velocity, (C2) is used. The longitudinal velocity of the satellite is most easily determined by using the fact that the total angular velocity of the satellite (in the satellite frame) is constant (ω_s). Then the longitudinal velocity of the satellite relative to the Earth is

$$\dot{\phi} = \omega_s \frac{\cos I}{\cos^2 \theta_c} - \omega_e. \quad (C9)$$

To establish the accuracy of these approximate satellite velocities, (C8) and (C9) were compared with the trajectory of a Geosat Exact Repeat Mission profile [Cheney et al., 1991]. The model velocities lie within 1 μ rad/s of the actual velocities [Sandwell, 1992]. The greatest error in total velocity occurs at 72° latitude where the difference is 7 m/s or 0.1%. Other numerical tests show that the position estimates from (C3) and (C7) are accurate to better than 1 km as long as the predicted position is less than 1/4 an orbit from the known equator crossing position.

Acknowledgments. We thank Bruce Douglas, Bob Cheney, Laury Miller, and Russ Agreen for their safe storage and distribution of the Geosat GM GDRs; no bytes were lost. ERS 1 data were provided by ESA through the French Processing and Archive Facility. Mara Yale supplied stacked profiles of Geosat ERM and ERS 1 data. Richard Eanes and C. K. Shum provided the software needed to compute the tide corrections. Steve Nerem provided the JGM-3 gravity field coefficients that were used as a reference model. Dick Rapp supplied software to construct the reference gravity model. Countless engineers and scientists worked to make both the Geosat and ERS 1 missions great successes. This paper benefited from the reviews of Steve Nerem and Anny Cazenave. This research was supported by the NASA Global Geophysics Program NAGW-3035 and UNOCAL Co.

References

- Andersen, O. B., P. Knudsen, and C. C. Tscherning, Investigation of methods for global gravity field recovery from the dense ERS-1 Geodetic Mission altimetry, paper presented at IUGG XXI General Assembly, Int. Union of Geol. and Geophys., Boulder, Colo., July, 1995.
- Bettadpur, S. V., and R. J. Eanes, Geographical representation of radial orbit perturbations due to ocean tides: Implications for satellite altimetry, *J. Geophys. Res.*, **99**, 24883-24898, 1994.
- Brammer, R. F., Estimation of the ocean geoid near the Blake Escarpment using Geos-3 satellite altimetry data, *J. Geophys. Res.*, **84**, 3843-3860, 1979.
- Briggs, I. C., Machine contouring using minimum curvature, *Geophysics*, **39**, 39-48, 1974.
- Cazenave, A., B. Parsons, and P. Calcagno, Geoid lineations of 1000 km wavelength over the Central Pacific, *Geophys. Res. Lett.*, **22**, 97-100, 1995.
- Cheney, R. E., N. S. Doyle, B. C. Douglas, R. W. Agreen, L. L. Miller, E. L. Timmerman, and D. C. McAdoo, *The Complete Geosat Altimeter GDR Handbook*, Natl. Geod. Surv./Natl. Oceanic and Atmos. Admin., Silver Spring, Md., 1991.
- Dumont, J. P., F. Ogor, and J. Stum, *Quality Assessment of Cersat Altimeter OPR Products: 168-Day Repeat Period*, French Processing and Archive Facility, Toulouse, France, 1995.
- Eanes, R. and S. Bettadpur, The CSR 3.0 global ocean tide model, Center for Space Research, Technical Memorandum, CSR-TM-95-06, 1995.
- Freedman, A. P., and B. Parsons, Seasat-derived gravity over the Musicians seamounts, *J. Geophys. Res.*, **91**, 8325-8340, 1986.
- Gille, S. T., Mean sea surface height of the Antarctic circumpolar current from Geosat data: Method and application, *J. Geophys. Res.*, **99**, 18255-18273, 1994.
- Haxby, W. F., and D. E. Hayes, Free-air gravity of the Southern Ocean derived from Seasat and Geosat altimeter data: Circum-Antarctic to 30°S, *Antarct. Res. Ser.*, vol. 54, *Marine Geological and Geophysical Atlas of the Circum-Antarctic to 30°S*, edited by D. E. Haynes, pp. 11-19 AGU, Washington, D.C., 1991.
- Haxby, W. F., G. D. Karner, J. L. Labrecque, and J. K. Weisell, Digital images of combined oceanic and continental data sets and their use in tectonic studies, *Eos Trans. AGU*, **64** (52), 995-1004, 1983.
- Haxby, W. F., and J. K. Weisell, Evidence for small-scale convection from Seasat altimeter data, *J. Geophys. Res.*, **91**, 3507-3520, 1986.
- Heiskanen, W. A., and H. Moritz, *Physical Geodesy*, W. H. Freeman, New York, 1967.
- Hwang, C., and B. Parsons, An optimal procedure for deriving marine gravity from multi-satellite altimetry, *J. Geophys. Int.*, **125**, 705-718, 1996.
- Hwang, C. W., and B. Parsons, Gravity anomalies derived from Seasat, Geosat, ERS-1 and Topex/Poseidon altimetry and ship gravity: A case study over the Reykjanes ridge, *Geophys. J. Int.*, **122**, 551-568, 1995.
- Jung, W. Y., and P. R. Vogt, Predicting bathymetry from Geosat-ERM and shipborne profiles in the South Atlantic Ocean, *Tectonophysics*, **210**, 235-253, 1992.
- Kaula, W. K., *Theory of Satellite Geodesy*, Blaisdel, Waltham, Mass., 1966.
- Laxon, S., and D. McAdoo, Arctic Ocean gravity field derived from ERS-1 satellite altimetry, *Science*, **265**, 621-624, 1994.
- Ma, X. C., C. K. Shum, R. J. Eanes, and B. D. Tapley, Determination of ocean tides from the first year of TOPEX/POSEIDON altimeter measurements, *J. Geophys. Res.*, **99**, 24809-24820, 1994.
- Marks, K. M., Resolution of the Scripps/NOAA marine gravity field from satellite altimetry, *Geophys. Res. Lett.*, **23**, 2069-2072, 1996.
- Marks, K. M., and R. V. Sailor, Comparison of Geos-3 and Seasat altimeter resolution capabilities, *Geophys. Res. Lett.*, **13**, 697-700, 1986.
- Marks, K. M., D. C. McAdoo, and W. H. F. Smith, *Marine Gravity Derived from Geosat*, Natl. Geophys. Data Cent., Boulder, Colo., 1993.
- Menke, W., Applications of the POCS inversion method to interpolating

- topography and other geophysical fields, *Geophys. Res. Lett.*, *18*, 435-438, 1991.
- Nerem, R. S., et al., Gravity model development for the TOPEX/POSEIDON: Joint gravity models 1 and 2, *J. Geophys. Res.*, *99*, 24421-24447, 1994.
- Neumann, G. A., D. W. Forsyth, and D. Sandwell, Comparison of marine gravity from shipboard and high-density satellite altimetry along the Mid-Atlantic Ridge, 30.5°-35.5°S, *Geophys. Res. Lett.*, *20*, 1639-1642, 1993.
- Noreus, J. P., Improved resolution of Geosat altimetry using dense sampling and polynomial adjusted averaging, *Int. J. Remote Sens.*, *16*, 2843-2862, 1995.
- Roest, W. R., Seafloor spreading pattern of the North Atlantic between 10° and 40°N, *Geol. Ultraiectina*, *48*, 1-121, 1987.
- Rummel, R., and R. H. N. Haagmans, Gravity gradients from satellite altimetry, *Mar. Geod.* *14*, 1-12, 1990.
- Sandwell, D. T., A detailed view of the South Pacific from satellite altimetry, *J. Geophys. Res.*, *89*, 1089-1104, 1984.
- Sandwell, D. T., Antarctic marine gravity field from high-density satellite altimetry, *Geophys. J. Int.*, *109*, 437-448, 1992.
- Sandwell, D. T., and B. Zhang, Global mesoscale variability from the Geosat exact repeat mission: Correlation with ocean depth, *J. Geophys. Res.*, *94*, 17971-17984, 1989.
- Smith, W. H. F., On the accuracy of digital bathymetric data, *J. Geophys. Res.*, *98*, 9591-9603, 1993.
- Smith, W. H. F., and D. T. Sandwell, Bathymetric prediction from dense satellite altimetry and sparse shipboard bathymetry, *J. Geophys. Res.*, *99*, 21803-21824, 1994.
- Smith, W. H. F., and D. T. Sandwell, Global comparison of gravity anomalies measured by ships and derived from dense satellite altimetry (abstract), *Eos Trans. AGU*, *76*(16), Spring Meet. Suppl., S89, 1995.
- Smith, W. H. F., and P. Wessel, Gridding with continuous curvature splines in tension, *Geophysics*, *55*, 293-305, 1990.
- Stewart, R. H., *Methods of Satellite Oceanography*, Univ. of Calif. Press, Berkeley, 1985.
- Tapley, B. D., D. P. Chambers, C. K. Shum, R. J. Eanes, J. C. Ries, and R. H. Stewart, Accuracy assessment of large-scale dynamic ocean topography from TOPEX/POSEIDON altimetry, *J. Geophys. Res.*, *99*, 24605-24617, 1994.
- Visser, P. N. A. M., K. F. Wakker, and B. A. C. Ambrosius, Dynamic sea surface topography from Geosat altimetry, *Mar. Geod.* *16*, 215-239, 1993.
- Wakker, K. F., M. C. Naeije, E. Wisse, R. Scharroo, P. Visser, and B. Ambrosius, Geosat and ERS-1 radar altimetry over the North Atlantic, *Adv. Space Res.*, *13*, 305-314, 1993.
- Watts, A. B., On geoid heights derived from Geos 3 altimeter data along the Hawaiian-Emperor seamount chain, *J. Geophys. Res.*, *84*, 3817-3826, 1979.
- Wessel, P., and W. H. F. Smith, New version of generic mapping tools, *Eos Trans. AGU Electron. Suppl.*, Aug. 15, 1995. (Available as http://www.agu.org/eos_elec/95154e.html)
- Wessel, P., and A. B. Watts, On the accuracy of marine gravity measurements, *J. Geophys. Res.*, *93*, 393-413, 1988.
- Yale, M. M., D. T. Sandwell, and W. H. F. Smith, Comparison of along-track resolution of stacked Geosat, ERS-1, and TOPEX satellite altimeters, *J. Geophys. Res.*, *100*, 15117-15127, 1995.

D. T. Sandwell, Scripps Institution of Oceanography, IGPP-0225, University of California, 9500 Gilman Drive, La Jolla, CA 92093-0225. (e-mail: sandwell@radar.ucsd.edu)

W. H. F. Smith, Geosciences Laboratory, NOAA, NOES-12, Silver Spring, MD 20910-3281. (e-mail: walter@amos.grd1.noaa.gov)

(Received June 3, 1996; revised October 11, 1996; accepted October 15, 1996.)